AIAA JOURNAL
Vol. 48, No. 2, February 2010

Aeroelastic Airfoil with Free Play at Angle of Attack with Gust Excitation

Deman Tang* and Earl H. Dowell†
Duke University, Durham, North Carolina 27708-0300

DOI: 10.2514/1.44538

A theoretical and experimental aeroelastic study of a typical airfoil section with control surface free play for nonzero angle of attack in low subsonic flow is presented. The study includes the flutter and limit cycle oscillation behavior and also the linear and nonlinear aeroelastic responses excited by periodic gust loads. The theoretical approach uses Peters's finite state airloads model. The experimental investigation has been carried out in the Duke University wind tunnel using a rotating slotted cylinder gust generator. The theoretical and experimental results show that the self-excited aeroelastic limit cycle oscillation is sensitive to the effect of initial pitch angle. For the gust response, the effect of initial pitch angle is smaller for the plunge and pitch responses and is larger for the flap response. The fair to good quantitative agreement between theory and experiment verifies that the present analytical approach has reasonable accuracy and good computational efficiency for nonlinear aeroelastic response analysis of such systems.

Nomenclature

b	=	semichord of the airfoil, $c/2$
C_a	=	aerodynamic damping matrix
C_e	=	damping matrix of aeroelastic model
C_s	=	structural damping matrix
c	=	chord of the airfoil
h	=	plunge displacement
K_a	=	aerodynamic stiffness matrix
K_e	=	stiffness matrix of aeroelastic model
K_s	=	structural stiffness matrix
K_β	=	flap stiffness
M_a	=	aerodynamic mass matrix
M_e	=	mass matrix of aeroelastic model
M_s	=	structural mass matrix
M_β	=	flap moment about the flap axis
t	=	time
U	=	freestream velocity
w_g	=	gust velocity
α	=	pitch angle of the airfoil
α_g	=	gust angle of attack
α_0	=	initial pitch angle of attack
β	=	flap rotational angle
Γ	=	total bound vorticity
Δp	=	pressure difference on the airfoil
δ	=	free-play region
λ	=	inflow velocity
ρ	=	air density
ω_g	=	gust oscillatory frequency
ω_h, ω_α	=	plunge and pitch natural frequency
ω_β	=	flap natural frequency

Received 23 March 2009; revision received 17 July 2009; accepted for publication 21 July 2009.

*Research Scientist, Department of Mechanical Engineering and Materials Science, Post Office Box 90300, Hudson Hall; demant@duke.edu. Member AIAA.

†William Holland Hall Professor, Department of Mechanical Engineering and Materials Science; also Dean Emeritus, Pratt School of Engineering, Post Office Box 90300, Hudson Hall; dowell@ee.duke.edu. Honorary Fellow AIAA (Corresponding Author).

I. Introduction

EARLY theoretical and experimental studies of 3-degree-of-freedom aeroelastic typical section with control surface free play have been discussed in the introduction of [1]. In the past few years at Duke University, the present authors and colleagues have constructed a typical airfoil section aeroelastic experimental model with control surface free play. They have also designed and installed an experimental rotating slotted cylinder (RSC) gust generator in the Duke University low-speed wind tunnel based upon a concept developed by W. H. Reed III. This gust generator is used to create a periodic or a linear frequency sweep gust excitation field. Using these experimental facilities, a series of theoretical and experimental studies of linear and nonlinear aeroelastic self-excited oscillations, that is, flutter and limit cycle oscillations (LCOs) [1–5], gust responses [6], gust alleviation [7,8], and flutter/LCO control [9–12] have been completed. These studies considered zero angle of attack for this aeroelastic system. Kholodar and Dowell [13] theoretically predicted the behavior of an airfoil with control surface free play for nonzero angle of attack using Theodorsen aerodynamic theory. They [13] demonstrated the significant effect of the initial pitch angle on the flutter/LCO behavior. Following our early studies, the goals of the present work are as follows:

1) We study the theoretical and experimental correlation of the flutter/LCO behavior when the initial pitch angle α_0 is not zero. In this work, the aerodynamic forces are based on Peters's finite state incompressible airloads model; see [14,15].

2) We study theoretically and experimentally the linear and nonlinear aeroelastic response to a periodic gust load for zero and nonzero angles of attack. The gust load spectrum used in the theoretical prediction is provided by the measured gust angle vs gust frequency.

In the present work, time marching has been used to produce the theoretical/computational results. However, as discussed in [3], considerable insight into the behavior of the system can be obtained by using a frequency domain, harmonic balance analysis. In particular, it can be shown that the minimum flow velocity at which LCO will occur is independent of the amount of free play. This is because the effective frequency of the control surface varies with amplitude of oscillation, and the LCO that occurs is determined by the control surface frequency that minimizes the classical flutter speed predicted by a traditional linear flutter analysis. At this flow velocity, the LCO amplitude will be that required to provide the control surface frequency that minimizes the flow velocity for the onset of flutter/LCO [3].

II. State-Space Theoretical Model

A. Aerodynamic Model

Peters's finite state incompressible airloads model for a deformable airfoil [14] is used to determine the aerodynamic forces. We consider a thin airfoil in a moving two-dimensional coordinate system (xoz) performing small motion $z(x, t)$ in the z direction and in the interval $-b \le x \le b$, as shown in Fig. 1. The nonpenetration boundary condition on the moving airfoil can be written as

$$v = U\partial z/\partial x + \partial z/\partial t + w_g(t) - \lambda \tag{1}$$

where v is the necessary induced flow in the negative z direction due to bound vorticity, λ is the downwash due to all induced flow, and $w_g(t)$ is a known lateral gust velocity time history.

The relationship between the v and the unknown bound vorticity γ_b is given as

$$v = \frac{-1}{2\pi}\int_{-b}^{b} \frac{\gamma_b(\xi, t)}{x - \xi}\,\mathrm{d}\xi \tag{2}$$

and the pressure difference across the airfoil is

$$\Delta p = \rho U\gamma_b + \rho\int_{-b}^{x} \frac{\partial\gamma_b}{\partial t}\,\mathrm{d}\xi \tag{3}$$

For the two-dimensional case of Fig. 1, the induced flow λ due to free vorticity is given by

$$\frac{\partial\lambda}{\partial t} + U\frac{\partial\lambda}{\partial x} = \frac{1}{2\pi}\frac{\partial\Gamma/\partial t}{b - x} \tag{4}$$

where Γ is the total bound vorticity on the airfoil

$$\Gamma \equiv \int_{-b}^{b} \gamma_b\,\mathrm{d}x \tag{5}$$

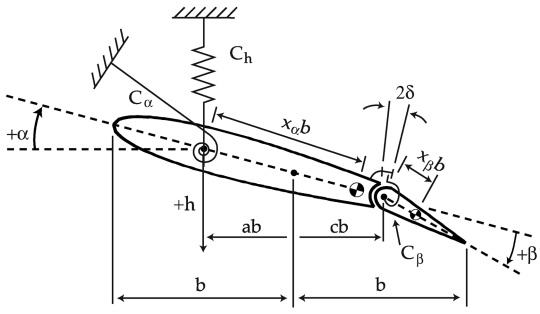

a)

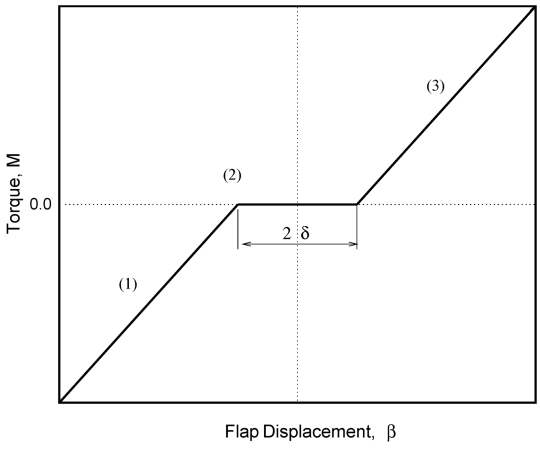

b)

Fig. 1 Thin airfoil in a moving two-dimensional coordinate system: a) sketch of the typical aeroelastic section with control surface, and b) restoring moment for the flap degree of freedom β with a symmetric free-play region about $\beta = 0$.

Using a Glauert variable ϕ, then

$$x = b\cos\phi \qquad -b \le x \le b, \qquad 0 \le \phi \le \pi \tag{6}$$

The appropriate expansions follow from thin airfoil theory:

$$\gamma_b = 2\left[\frac{\gamma_s}{\sin\phi} - \frac{\gamma_0\cos\phi}{\sin\phi} + \sum_{n=1}^{\infty}\gamma_n\sin(n\phi)\right] \tag{7}$$

$$\Delta p = 2\rho\left[\frac{\tau_s}{\sin\phi} - \frac{\tau_0\cos\phi}{\sin\phi} + \sum_{n=1}^{\infty}\tau_n\sin(n\phi)\right] \tag{8}$$

Following Eqs. (2), (7), and (8), we have

$$v = \sum_{n=0}^{\infty}\gamma_n\cos(n\phi) \tag{9}$$

$$\lambda = \sum_{n=0}^{\infty}\lambda_n\cos(n\phi) \tag{10}$$

$$z = \sum_{n=0}^{\infty}h_n\cos(n\phi) \tag{11}$$

where the generalized airfoil motion h_n for a special case of a rigid-body airfoil can represent a matrix form in terms of airfoil degrees of freedom h, α, and β. It is

$$\{h_n\} = [T]\begin{Bmatrix} h \\ \alpha \\ \beta \end{Bmatrix} \tag{12}$$

The lateral gust velocity is expanded as follows:

$$w_g = \sum_{n=0}^{\infty}w_{gn}\cos(n\phi) \tag{13}$$

From the preceding equations, generalized forces associated with each generalized airfoil motion h_n and the generalized gust loads w_{gn} can be obtained. They are

$$L_n = -\int_{-b}^{b}\Delta p\cos(n\phi)\,\mathrm{d}x = -\int_{0}^{\pi} b\Delta p\cos(n\phi)\sin\phi\,\mathrm{d}\phi \tag{14}$$

B. Aeroelastic Model

The structural model is standard and is discussed in [1].

Defining a state vector $X_e = \{\dot{h}, \dot{\alpha}, \dot{\beta}, h, \alpha, \beta, \lambda\}^T$, we obtain a set of state-space equations with six structural states and N inflow states. These equations are

$$\dot{X}_e = A_e X_e + B_e \tag{15}$$

where

$$A_e = \begin{bmatrix} M_e & C_e & 0 \\ 0 & M_e & 0 \\ -B_1 & -\frac{U}{b}B_2 & A \end{bmatrix}^{-1}\begin{bmatrix} 0 & -K_e & B_n \\ M_e & 0 & 0 \\ 0 & 0 & -\frac{U}{b}I \end{bmatrix}$$

and

$$B_e = \begin{bmatrix} M_e & C_e & 0 \\ 0 & M_e & 0 \\ -B_1 & -\frac{U}{b}B_2 & A \end{bmatrix}^{-1} \times \left(\begin{Bmatrix} 0 \\ -M_\beta \\ 0 \end{Bmatrix} + [G_{e1}]\{w_{gn}\} + [G_{e2}]\{\dot{w}_{gn}\} \right)$$

where submatrices M_e, K_e, and C_e are the equivalent mass, stiffness, and damping matrices composed of structural (M_s, K_s, C_s) and aerodynamic components (M_a, K_a, C_a), $M_e = [M_s] + [M_a]$, $C_e = [C_s] + [C_a]$, $K_e = [K_s] + [K_a]$, and the submatrix B_n is determined using an equation of the form

$$\lambda_0 = \frac{1}{2}\sum_{n=1}^{N} b_n \lambda_n$$

and is given in [15]. The matrices B_1, B_2, $[G_{e1}]$, and $[G_{e2}]$ are given in [6].

The structural stiffness matrix $[K_s]$ is given by

$$[K_s] = \begin{bmatrix} K_h & 0 & 0 \\ 0 & K_\alpha & 0 \\ 0 & 0 & \nu K_\beta \end{bmatrix}$$

When the structural free-play gap δ is zero, then $\nu = 1$ and $M_\beta = 0$, and when the structural free-play gap is not zero, then $\nu = 0$ and the control surface moment-rotation relationships may be expressed as

$$M_\beta = \begin{cases} K_\beta(\beta - \delta)|\beta| \geq \delta, & \beta > 0 \\ K_\beta(\beta + \delta)|\beta| \geq \delta, & \beta < 0 \\ 0 & \text{otherwise} \end{cases} \tag{16}$$

The aerodynamic stiffness matrix K_a is a function of the initial pitch angle α_0.

III. Theoretical and Experimental Correlations

A. Results from Preliminary Wind-Tunnel Test

A 3-degree-of-freedom aeroelastic typical section with control surface free play is modeled experimentally. The experimental model, measurement system, and data acquisition are described in [1]. The experimental model is mounted in a vertical position in the center of the test section. A gust generator is mounted upstream of the experimental model. The gust was created by placing a rotating slotted cylinder behind a rigid airfoil upstream of the aeroelastic airfoil wing model. The gust generator configuration in the wind tunnel had two airfoils or vanes and two rotating slotted cylinders. The distance between these vanes was 12 in. A photograph of the experimental model with the gust generator in the wind-tunnel model is shown in Fig. 2. For details of the gust generator design, see [16].

Fig. 2 Photograph of the experimental model with gust generator in the wind-tunnel test.

Table 1 Model parameters

Model parameters	
Chord	0.254 m
Span	0.52 m
Semichord (Fig. 1a, segment b)	0.127
Elastic axis (Fig. 1a, segment ab)	−0.5
Hinge line (Fig. 1a, segment cb)	0.5
Mass parameters	
Mass of wing	0.713 kg
Mass of aileron	0.18597 kg
Mass/length of wing aileron	1.73 kg/m
Mass of support blocks	0.467 × 2 kg
Total mass per span, M_h	3.625 kg/m
Inertial parameters	
S_α, per span	0.0726 kg
S_β, per span	0.00393 kg
I_α, per span	0.0185 kgm
I_β, per span	0.00025 kgm
Stiffness parameters	
K_α, per span	46.88 kgm/s^2
K_β, per span	2.586 kgm/s^2
K_h, per span	2755.4 kg/ms^2
Damping parameters	
ζ_α, half-power	0.0175
ζ_β, half-power	0.032
ζ_h, half-power	0.0033

The system parameters for the experimental model are shown in Table 1. These differ slightly from those of [1–4] and this in turn leads to modest differences in the aeroelastic response.

A preliminary test of the flutter/LCO model was used to determine the natural frequencies and the modal damping of the coupled structure and individual component motion (plunge, pitch, and flap motions) of this experimental model. There are four major components of the vibration test: excitation, measurement, recording, and analysis. An autosweeping sinusoidal signal is provided by an SD 380 signal analyzer. A minishaker BK-4810 and power amplifier BK-2706 are used to excite the model. The drive point is placed at the upper support block. A force transducer BK-8200 is used to measure the force at the joint between the minishaker and the model. A charge amplifier BK-2635 is used to provide signal conditioning and amplification of the force signal.

The output response signals include the plunge displacement, pitch angle of the main wing, and flap rotational motion from the three transducers. They are connected to the SD 380 input channels. A transfer function analysis between the input force and output responses is completed by the SD 380 for the frequency range 0–20 Hz. A photograph of the ground vibration test is shown in Fig. 3. From the transfer function, the coupled natural frequencies for the pitch, plunge, and flap motion were determined. In addition to the three primary degrees of freedom, the experimental model has the potential to exhibit a fourth degree of freedom (roll) due to out-of-phase plunging motion between the upper and lower support. A typical transfer function plot is shown in Fig. 4. Figure 4a shows the phase angle between the input (force) and output (flap motion), and Fig. 4b shows the magnitude of the transfer function β/F. As shown in this figure, There are four primary natural frequencies. The peak at frequency of 12 Hz is rolling motion.

From the experimental results, a comparison of the structural natural frequencies for the numerical and experimental systems is given in Table 2. Also shown are the flutter velocity for no free play. Once the linear flutter velocity for no free play is exceeded, the response is an exponentially increasing oscillation, whatever the amount of free play.

B. Results for the Flutter/Limit Cycle Oscillation

All flutter/LCO and gust response tests of the two-dimensional wing model with control surface free play were performed in the Duke University low-speed wind tunnel. The wind tunnel is a closed circuit tunnel with a test section of 0.701 × 0.506 m and a length of 1.219 m. The maximum attainable air speed is 89 m/s. The

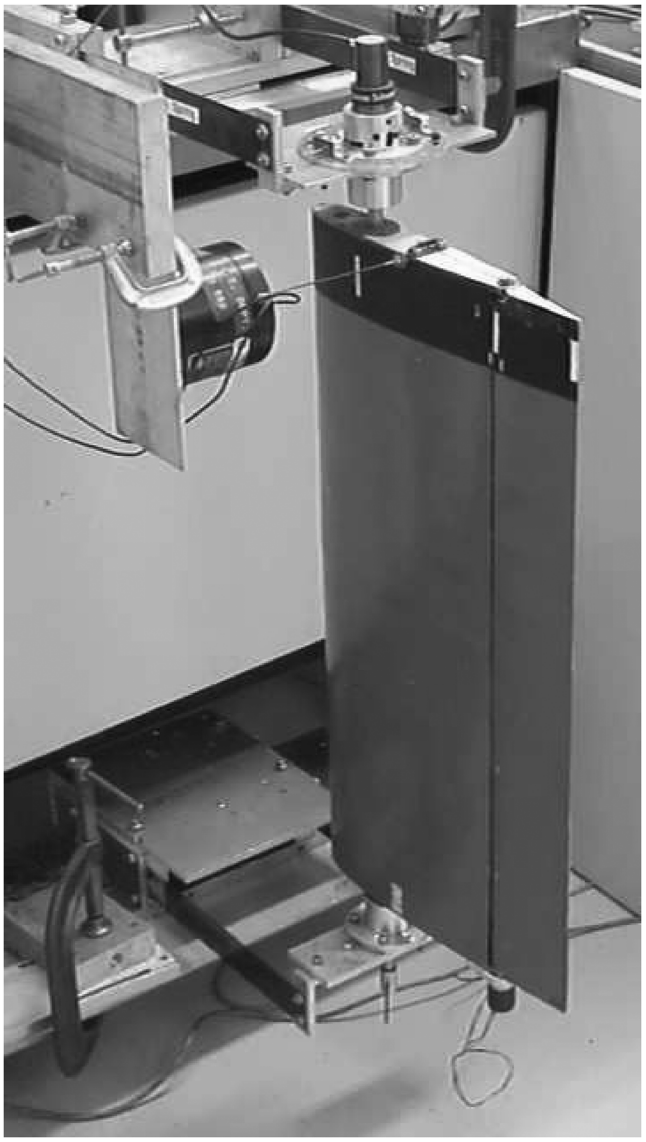

Fig. 3 Photograph of the experimental model in the ground vibration test.

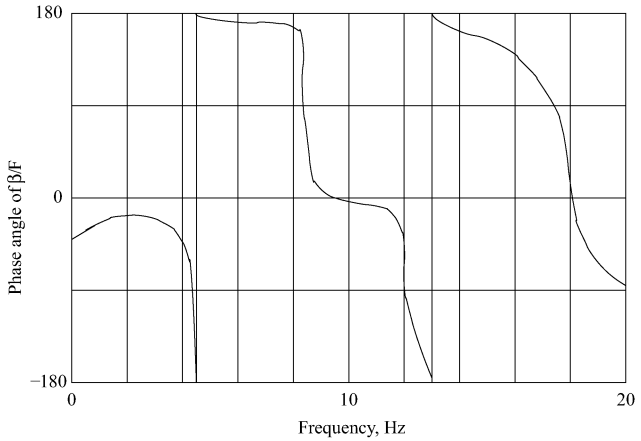

a) Phase angle of β/F

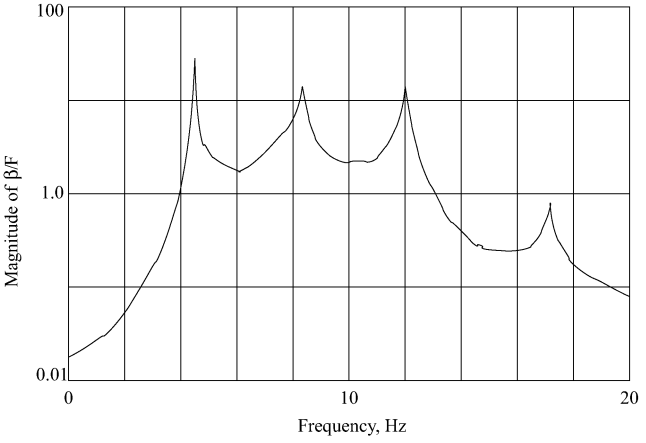

b) Magnitude of β/F

Fig. 4 Experimental transfer function between the input force and flap response motion of the wind tunnel model: a) phase angle, b) magnitude.

stagnation temperature of the airstream is held constant over the range of 15–38° C by means of an external air-exchange system, and tunnel stagnation pressure equals the atmospheric pressure at the low Reynolds number operating conditions. For the present test, the Reynolds number based upon model chord was 0.52×10^6.

When the free-play gap is set zero, the measured flutter flow velocity is 26.5 m/s for zero initial angle of attack. Because in this flow velocity range the model motion is very large, we use an external device to limit the plunge motion amplitude. The measured flutter frequency is about 6.25 Hz. For the theoretical prediction of the linear flutter, we set matrix B_e in Eq. (15) to be zero and then to solve the eigenvalues of this matrix equation. The flutter velocity and frequency can be determined from these eigenvalues. The theoretical and experimental correlation of flutter velocity and frequency for the linear airfoil wing model is also shown in Table 2.

For the flutter/LCO test, a free-play gap $2 \times \delta = 2 \times 2.12$ deg is to be used. The initial angle of attack is varied over a range of values $\alpha_0 = 0$, 2, 4, 6, and 8 deg. The initial conditions of both the computations and the experiments are described in Sec. III.C.

The experimental amplitudes shown are based on root-mean square (rms) calculations over several complete cycles of the experimental steady-state time histories. Nonzero static equilibrium points are found for nonzero angles of attack, but a discussion of these is omitted here for the sake of brevity. Only dynamic oscillations about such static points are reported.

A nondimensional rms amplitude normalized by the free-play gap is introduced here. The pitch and flap motions are nondimensionalized by the free-play gap, that is, by $2 \times \delta$. For the plunge motion, it is nondimensionalized by $2 \times \pi\delta b/180$ deg.

For comparison with the experimental data, two theoretical methods are used. One is a simple aeroelastic model from Eq. (15) conducted by Duke. The other applies the ZAERO code conducted by ZONA Technology, Inc. Both results are plotted in Figs. 5–9. (The gust responses are shown later.)

Figures 5 shows the nondimensional plunge, pitch, flap LCO amplitudes, and LCO frequency vs the flow velocity for the initial pitch angle $\alpha_0 = 0$. The motion may be periodic or nonperiodic or chaotic. Here, we use rms amplitude to present the LCO motion vs the flow velocity.

As shown in Fig. 5, when the flow velocity U is less than 4.67 m/s, no LCO occurs both for the theory and experiment. When U is between 4.67 and 13.26 m/s for the experiment and 4.55 and 14.1 m/s for the theory, the motion is dominated by the plunge degree of freedom and has an oscillation frequency of about 4.5–5 Hz for both the theory and experiment. When U is between 13.26 and 25.6 m/s for the experiment and 14.1 and 27.4 m/s for the theory,

Table 2 Model natural frequencies

	Computational	Experimental	% difference
ω_α, coupled	8.32 Hz	8.45 Hz	1.6
ω_β, coupled	17.64 Hz	17.37 Hz	1.5
ω_h, coupled	4.37 Hz	4.45 Hz	1.83
U_F, m/s	27.3	26.5	2.9
ω_F, Hz	6.05	6.25	3.3

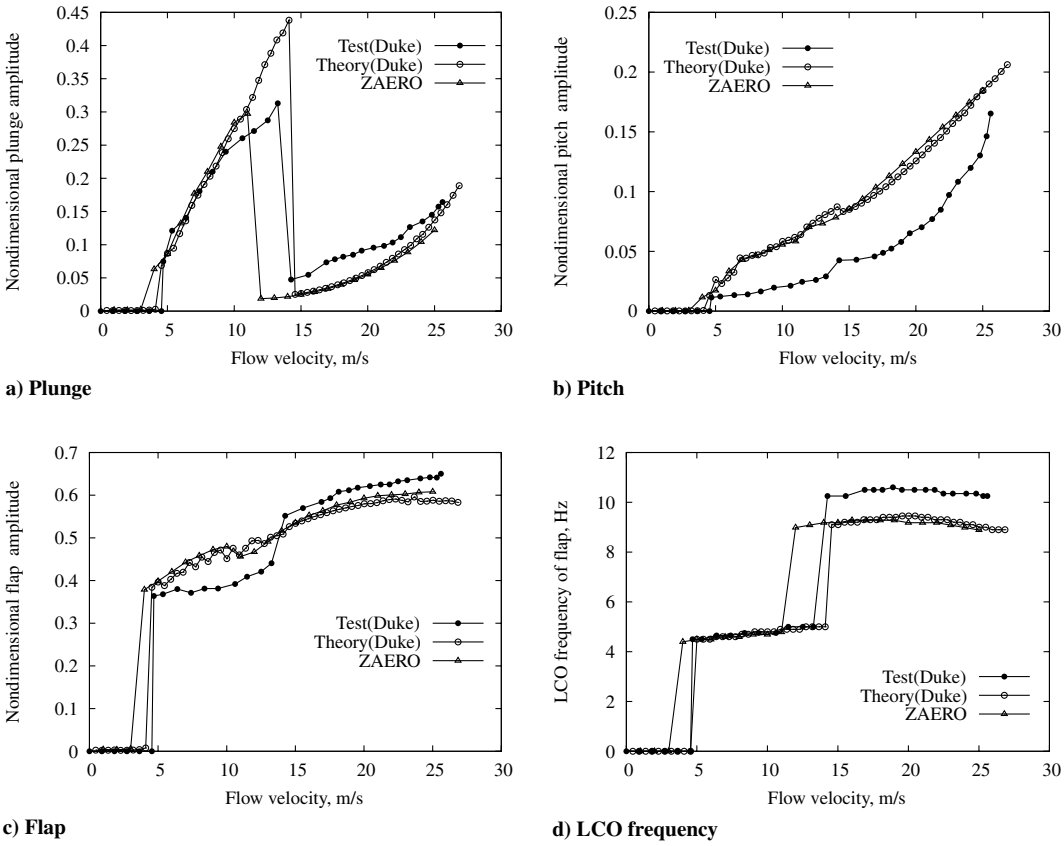

Fig. 5 Theoretical and experimental LCO rms response amplitudes and frequency for the initial pitch angle of $\alpha_0 = 0$ deg and $\delta = 2.12$ deg.

the motion is dominated by the flap degree of freedom and has an oscillation frequency of about 10–10.5 Hz for the experiment and 9–9.5 Hz for the theory. When U is greater than 25.6 m/s, the experimental LCO amplitude abruptly increases and the test is stopped to protect the model (this is called the catastrophic flutter velocity). This flow velocity is close to the experimental flutter velocity (26.5 m/s) of the linear structure without free play. However, the theoretical catastrophic flutter velocity is 27.4 m/s and is slightly higher than the theoretical linear flutter velocity (27.3 m/s). The quantitative agreement between the theory and experiment is reasonably good.

Figure 6 shows the nondimensional plunge, pitch, flap LCO amplitudes, and LCO frequency vs the flow velocity for $\alpha_0 = 2$ deg. When U is between 4.67 and 13.12 m/s for the experiment and 4.55 and 13.65 m/s for the theory, the motion is dominated by the plunge degree of freedom and has an oscillation frequency of about 4.5–5 Hz for both the theory and experiment. When U is between 13.12 and 25.05 m/s for the experiment and 13.65 and 27.3 m/s for the theory, the motion is dominated by the flap degree of freedom and has an oscillation frequency of about 10–11.5 Hz for the experiment and 9–9.5 Hz for the theory. At $U = 14.56$ m/s for the theory, there is jump from a higher frequency oscillation (9.06 Hz) to a lower frequency oscillation (5 Hz). When U is greater than 25.05 m/s, the experimental LCO amplitude abruptly increases and the catastrophic flutter velocity is 25.05 m/s. The theoretical catastrophic flutter velocity is equal to the theoretical linear flutter velocity (27.3 m/s). For comparison, the computational results using the computational fluid dynamics code ZAERO, provided by ZONA Technology, Inc., are also presented in Figs. 5–9. The quantitative agreement between the theory and experiment is reasonably good.

Note that, in Fig. 6, there is a downward spike in the response near 14 m/s. This occurs near the transition from one LCO to another. This transition is sensitive to the initial conditions chosen and other choices would eliminate or move the flow velocity at which such a spike may occur.

Similar results are shown in Figs. 7–9 for $\alpha_0 = 4$, $\alpha_0 = 6$, and $\alpha_0 = 8$ deg, respectively. The following observations may be made.

1) The flow velocity corresponding to a change in the LCO behavior from a lower frequency oscillation to a higher frequency oscillation changes modestly in the experiments as α_0 increases. For the test, these flow velocities are 13.26 m/s for $\alpha_0 = 0$ deg, 13.12 m/s for $\alpha_0 = 2$ deg, 12.5 m/s for $\alpha_0 = 4$ deg, and 10.5 m/s for $\alpha_0 = 6$ deg. For $\alpha_0 = 8$ deg, the LCO for the higher frequency oscillation has disappeared at the flow velocities $U = 9.8$ m/s. For the theory, these flow velocities are 14.1 m/s for $\alpha_0 = 0$ deg, 13.65 m/s for $\alpha_0 = 2$ deg, and 13.63 m/s for $\alpha_0 = 4$ deg. For $\alpha_0 = 6$ and 8 deg, the LCO for the higher frequency oscillation has disappeared at the flow velocities $U = 12.28$ m/s and $U =$ 8.64 m/s, respectively, in the theoretical model. Also note that this disappearance occurs at around 24 m/s for 2 deg and 19 m/s for 4 deg in the theory and 22 m/s for 4 deg in the experiment.

2) The flow velocity corresponding to catastrophic flutter (very large LCO amplitude) also decreases as the initial pitch angle increases. The experimental results are 25.6 m/s for $\alpha_0 = 0$ deg, 25.05 m/s for $\alpha_0 = 2$ deg, 23.96 m/s for $\alpha_0 = 4$ deg, 21.48 m/s for $\alpha_0 = 6$ deg, and 20.43 m/s for $\alpha_0 = 8$ deg. However, for the theoretical predictions, the catastrophic flutter velocity is almost independent of the α_0 values.

3) When $\alpha_0 = 8$ deg, the flow velocity range for the LCO becomes quite small and when $\alpha_0 > 8$ deg, the LCO disappears both for the theory and test.

For additional insight into the LCO behavior with $\alpha_0 = 2$ deg and $\delta = 2.12$ deg, we present the theoretical and experimental time histories and fast Fourier transform (FFT) analysis of the plunge and flap motion for the flow velocities $U = 10.5$ and 20.22 m/s. These results are shown in Figs. 9 and 10. As shown in Fig. 9 for $U = 10.5$ m/s, both the plunge and flap motion have a larger oscillation with the dominant frequency $\omega = 4.9$ Hz (near the plunge natural frequency). There is a small difference between the theory and experiment for this frequency component. In addition to this dominant frequency component, the higher-order harmonic components are also shown in this figure.

As shown in Fig. 11 for $U = 20.22$ m/s, the flap motion has a larger oscillation with the dominant frequency $\omega = 9.1$ Hz for the

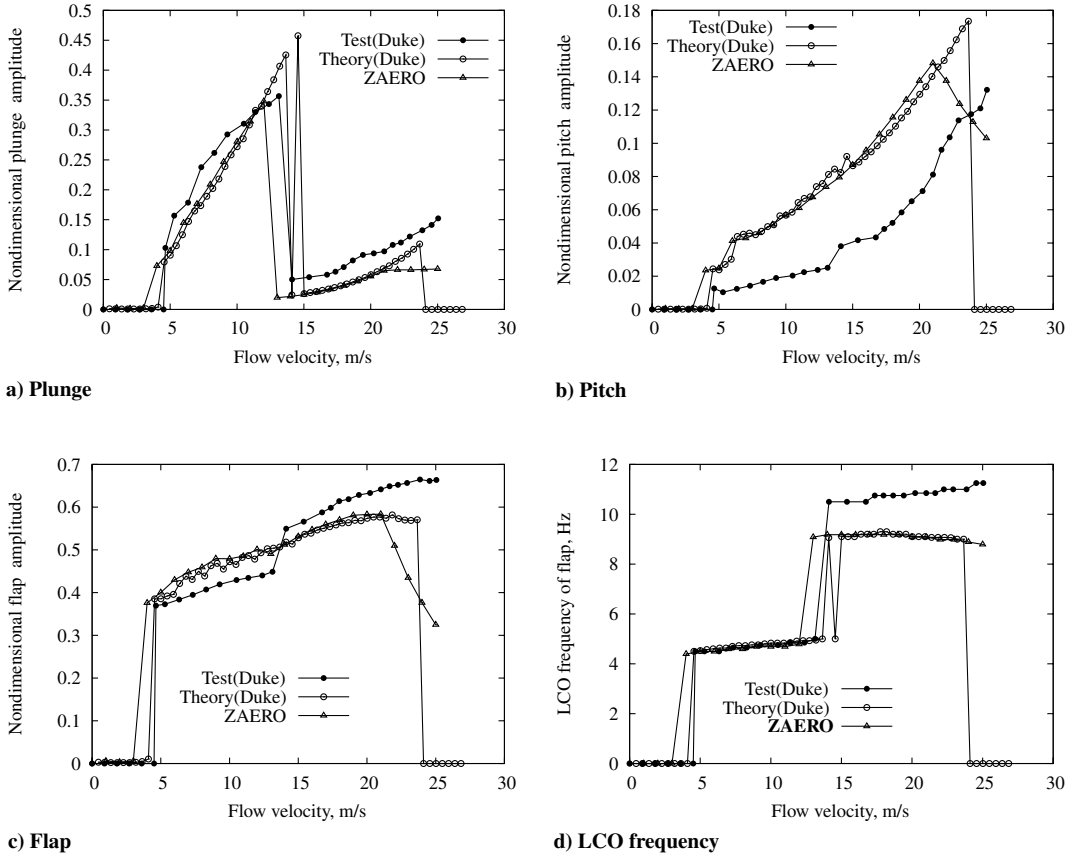

Fig. 6 Theoretical and experimental LCO rms response amplitudes and frequency for the initial pitch angle of $\alpha_0 = 2\,\mathrm{deg}$ and $\delta = 2.12\,\mathrm{deg}$.

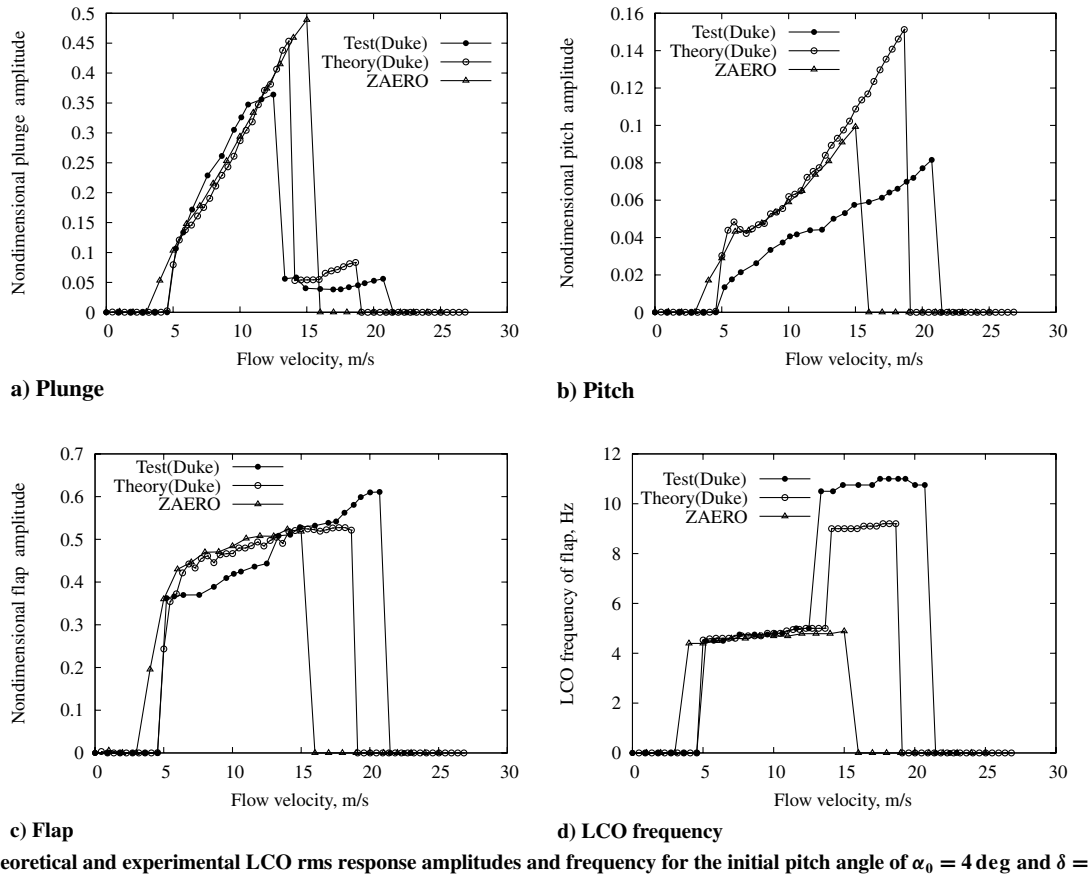

Fig. 7 Theoretical and experimental LCO rms response amplitudes and frequency for the initial pitch angle of $\alpha_0 = 4\,\mathrm{deg}$ and $\delta = 2.12\,\mathrm{deg}$.

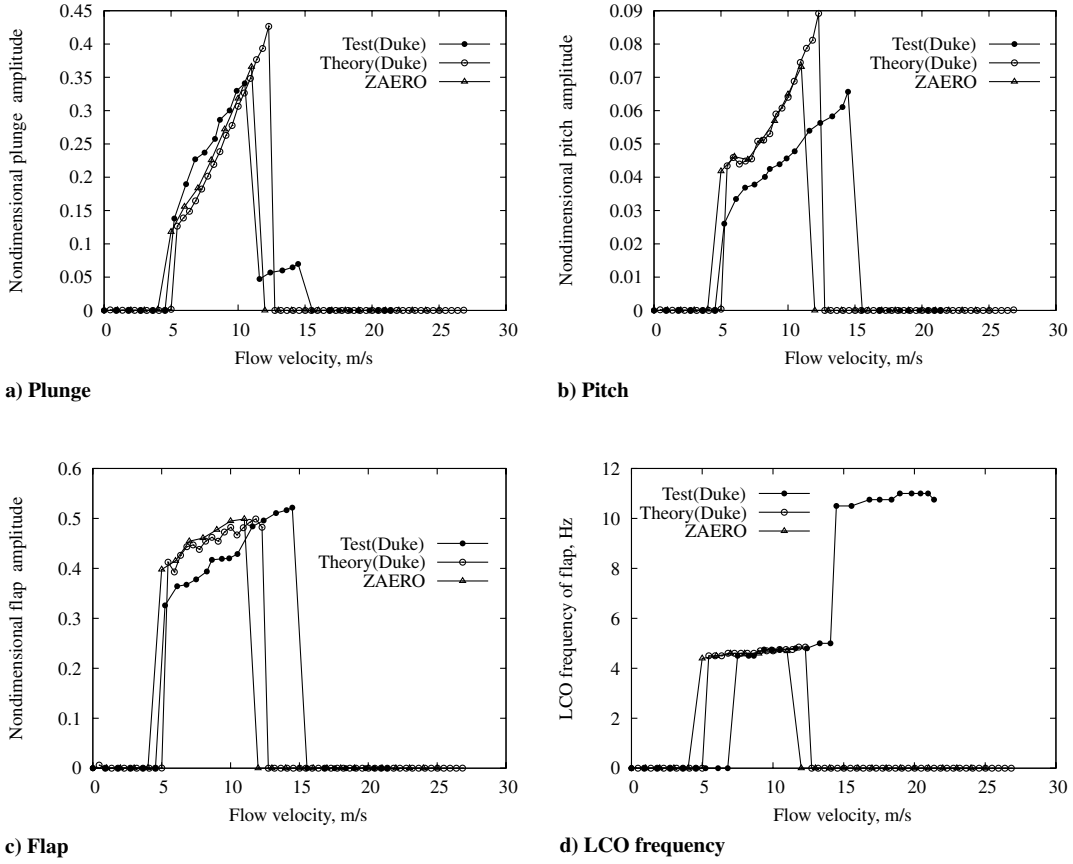

a) Plunge **b) Pitch**

c) Flap **d) LCO frequency**

Fig. 8 Theoretical and experimental LCO rms response amplitudes and frequency for the initial pitch angle of $\alpha_0 = 6\,\mathrm{deg}$ and $\delta = 2.12\,\mathrm{deg}$.

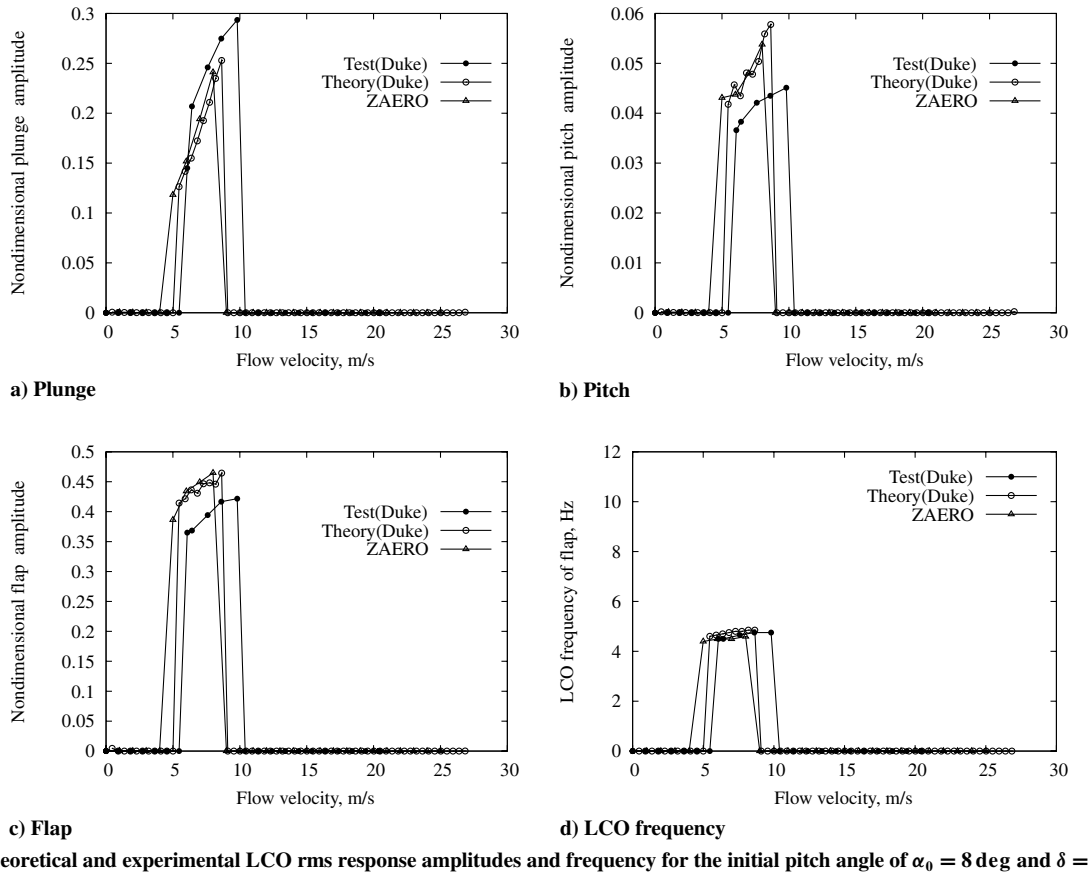

a) Plunge **b) Pitch**

c) Flap **d) LCO frequency**

Fig. 9 Theoretical and experimental LCO rms response amplitudes and frequency for the initial pitch angle of $\alpha_0 = 8\,\mathrm{deg}$ and $\delta = 2.12\,\mathrm{deg}$.

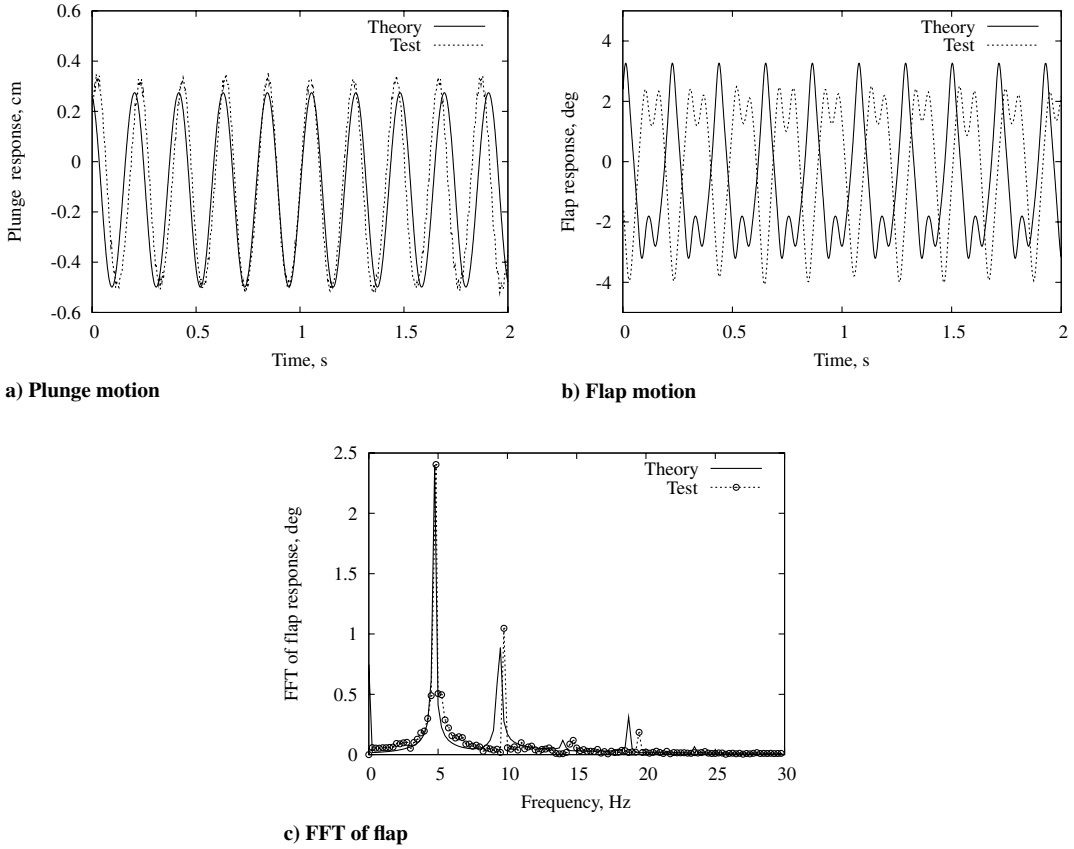

Fig. 10 Plunge and flap motion: a–b) theoretical and experimental time histories, and c) FFT analysis of flap response for a free-play angle of $\delta = 2.12$ deg and initial pitch angle $\alpha_0 = 2$ deg, and the flow velocity $U = 10.5$ m/s.

theory and 10.85 Hz for the experiment. However, the plunge motion is smaller. There is a larger difference between the theory and experiment for this frequency component.

Overall, the theory and experiment are in reasonable agreement with the largest differences at angles of attack in the midrange between zero and the angle of attack required to suppress LCO completely.

Because the airfoil section (NACA 0012) is symmetrical, the responses for $\pm\alpha_0$ should be the same. The free-play angle was set at $\delta = 2.12$ deg and $\alpha_0 = 2$ deg and $\alpha_0 = -2$ deg. Note that the initial conditions for $\alpha_0 = -2$ deg are set to be negative values of the original initial conditions. The results are shown in Figs. 12a–12d for the nondimensional amplitude. The two results are quite close. Any differences may be due to a small measurement error and a small uncertainty in the set of $\pm\alpha_0$ (i.e., the value of α_0 is not exactly equal to the value of $-\alpha_0$).

C. Effects of Initial Conditions on Limit Cycle Oscillations for Different Free-Play Gaps

Trickey et al. [4] conducted seminal studies of the effect of initial conditions on a similar free-play model and discovered some of the subtle aspects of nonunique LCO behavior, including chaos over narrow flow velocity ranges. The present work expands the database and our awareness of the ubiquity of multiple LCO that may occur over a broader range of flow velocities.

1) The initial plunge displacement is $h(t = 0) = 0.2$ cm, pitch angle is $\alpha(t = 0) = 2$ deg, flap angle is $\beta(t = 0) = 0$ deg, and the initial plunge, pitch, flap velocities, and aerodynamic inflow velocities are set to be zero for each flow velocity. All of the theoretical results from Figs. 5–12 of LCO response are based on these initial conditions. This is called the case of I.C.1.

2) For first flow velocity (onset of LCO state), the initial conditions are the same as for the case of I.C.1. For the next flow velocity (increasing ΔU), we use as initial conditions the final LCO conditions that are provided by the preceding LCO state. This process is continuous in time until the flow velocity increases to 27.3 m/s (linear flutter velocity). This is called the case of I.C.2.

Two free-play gaps, $2 \times \delta = 2 \times 1.06$ deg and $2 \times \delta = 2 \times 2.12$ deg, are considered for I.C.2. Also, two typical initial pitch angles are considered for I.C.2. One is a lower initial pitch angle, $\alpha_0 = 1$ deg for $\delta = 1.06$ deg and $\alpha_0 = 2$ deg for $\delta = 2.12$ deg; the other is a higher initial pitch angle, $\alpha_0 = 3$ deg for $\delta = 1.06$ deg and $\alpha_0 = 6$ deg for $\delta = 2.12$ deg.

To compare the rms amplitude for different free-play gaps, the plunge, pitch, and flap motions are nondimensionalized by the free-play gap described as before. Figure 13 shows the nondimensional plunge, pitch, flap LCO amplitudes, and LCO frequency vs the flow velocity for the initial pitch angle $\alpha_0 = 2$ deg for free-play angle $\delta = 2.12$ deg and the initial pitch angle $\alpha_0 = 1$ deg for free-play angle $\delta = 1.06$ deg. Comparing Fig. 13 (for I.C.2) to Fig. 6 (for I.C.1) for the lower initial pitch angle, there is a modest quantitative difference for the different initial conditions used (I.C.1 and I.C.2). The flow velocity corresponding to a change in the LCO behavior from a lower to higher frequency oscillation is similar for both initial conditions and correlates well with experiment.

For the initial pitch angle $\alpha_0 = 6$ deg for free-play angle $\delta = 2.12$ deg and the initial pitch angle $\alpha_0 = 3$ deg for free-play angle $\delta = 1.06$ deg, the theoretical and experimental results are shown in Fig. 14. Comparing Fig. 14 (for I.C.2) to Fig. 8 (for I.C.1) for the higher initial pitch angle, there is a significant quantitative difference for the different initial conditions used. The flow velocity corresponding to a change in the LCO behavior from a lower to higher frequency oscillation has only a small change. However, there is a significant difference for the flow velocity corresponding to the zero response in the experiments. This is $U = 14.48$ m/s for the case of I.C.1 and $U = 21.38$ m/s for the case of I.C.2.

In Figs. 13 and 14, the experimental initial conditions (I.C.2) appear to be similar to the theoretical case, but apparently are not exactly the same due to different LCO responses. The effects of initial conditions on LCO behavior are quite sensitive both for the lower and

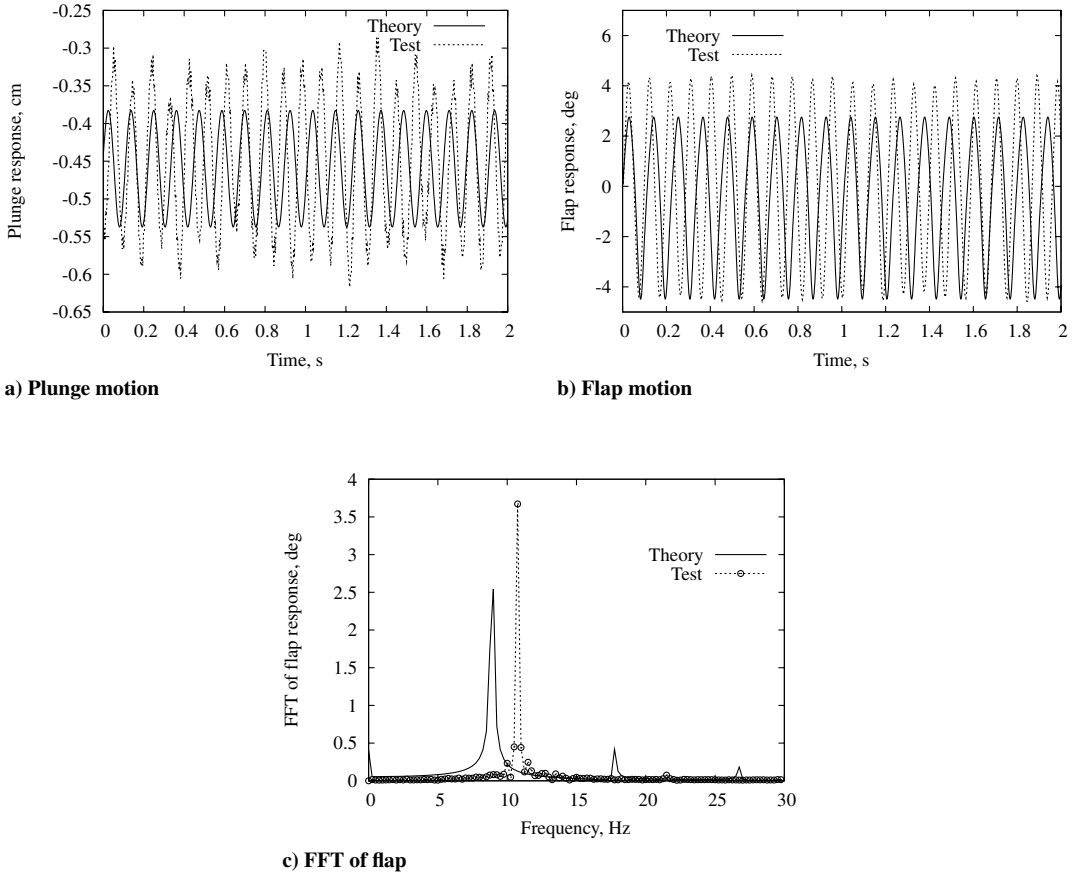

Fig. 11 Plunge and flap motion: a–b) theoretical and experimental time histories, and c) FFT analysis of flap response for a free-play angle of $\delta = 2.12\,\mathrm{deg}$ and initial pitch angle $\alpha_0 = 2\,\mathrm{deg}$, and the flow velocity $U = 20.22\ \mathrm{m/s}$.

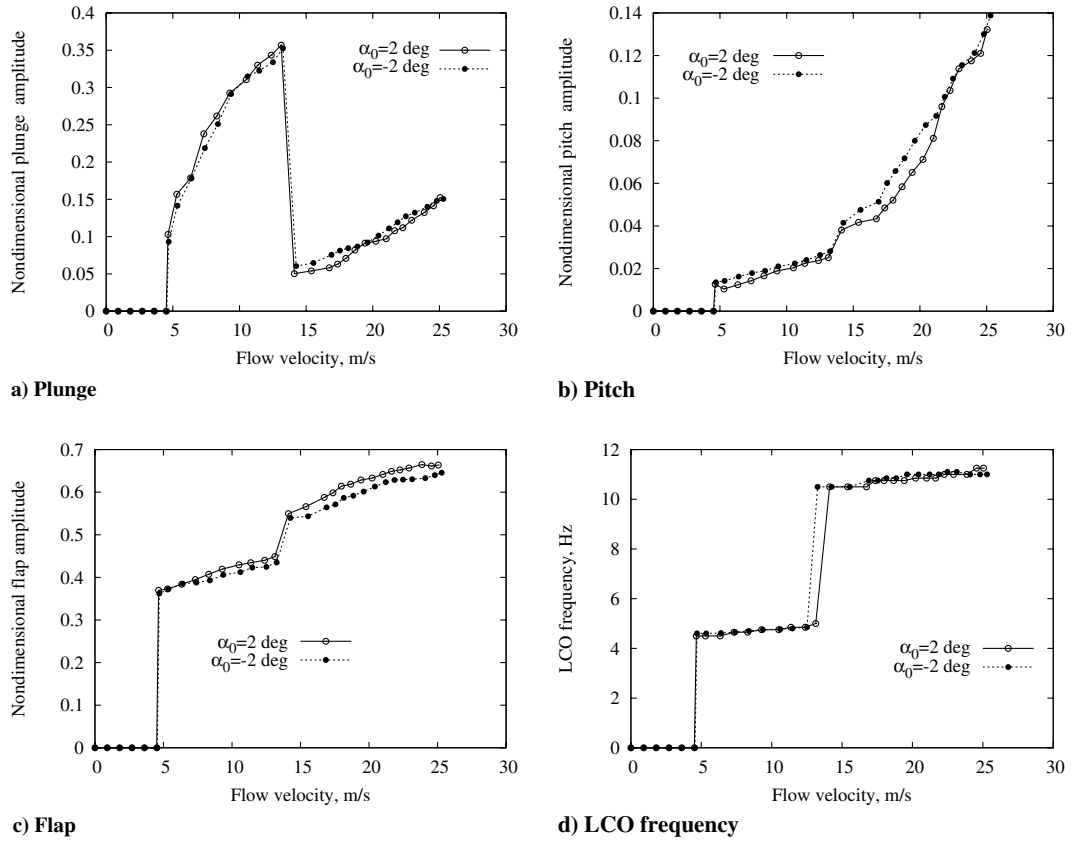

Fig. 12 Experimental comparative test for LCO rms response amplitudes and frequency in the case of $\delta = 2.12\,\mathrm{deg}$ and $\alpha_0 = \pm 2\,\mathrm{deg}$.

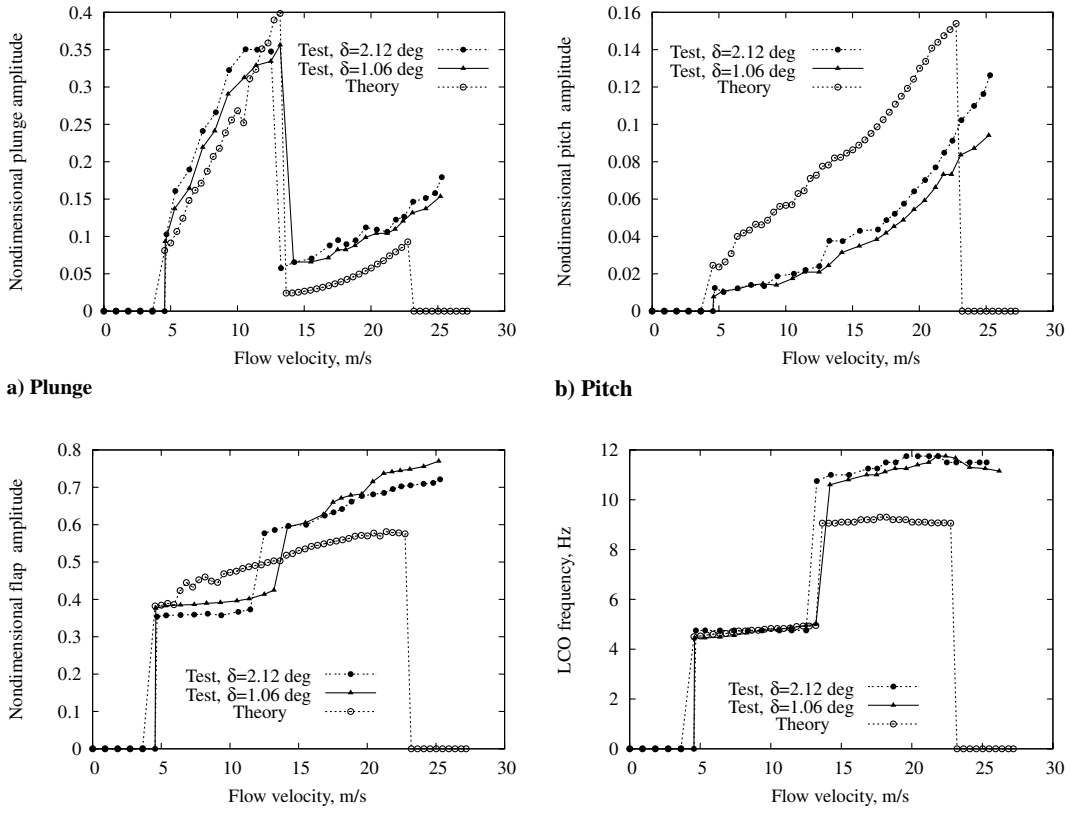

Fig. 13 Theoretical and experimental LCO rms response amplitudes and frequency for the initial pitch angle $\alpha_0 = 2\,\text{deg}$ for $\delta = 2.12\,\text{deg}$ and $\alpha_0 = 1\,\text{deg}$ for $\delta = 1.06\,\text{deg}$.

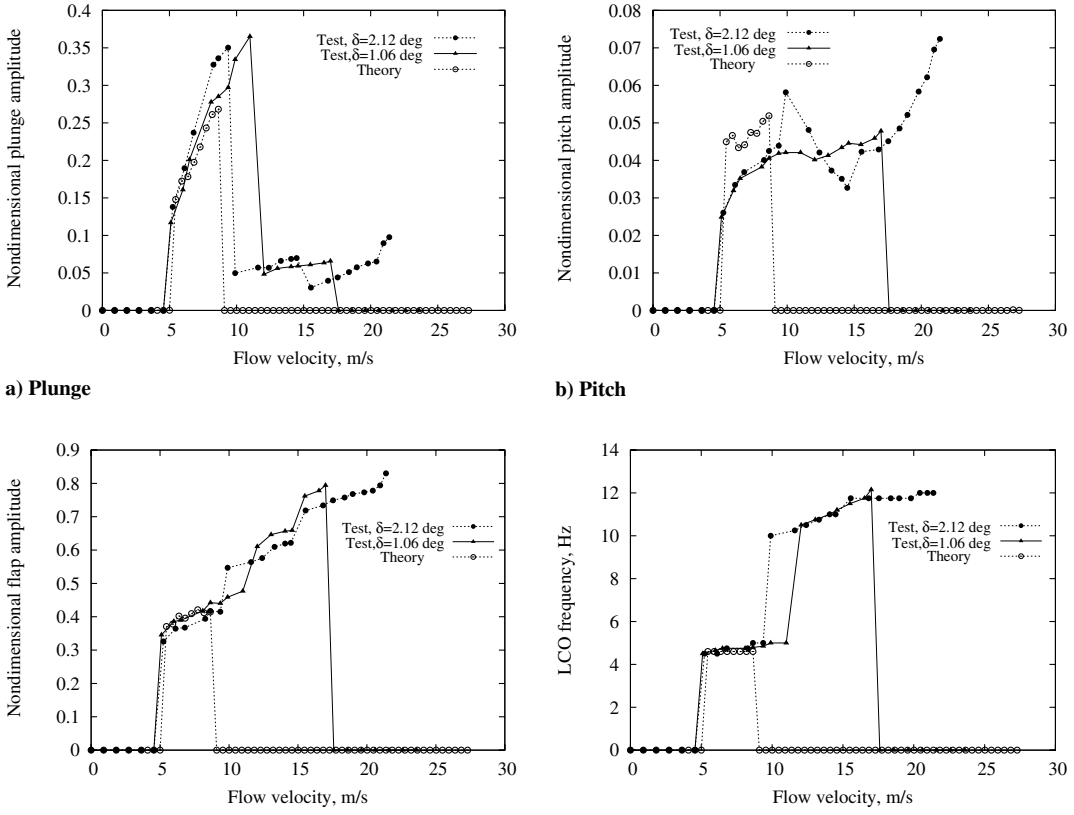

Fig. 14 Theoretical and experimental LCO rms response amplitudes and frequency for the initial pitch angle $\alpha_0 = 6\,\text{deg}$ for $\delta = 2.12\,\text{deg}$ and $\alpha_0 = 3\,\text{deg}$ for $\delta = 1.06\,\text{deg}$.

higher pitch angles α_0 when the flow velocity is high enough. For $U \leq 12$–14 m/s, the LCO that is present for these lower velocities is unique and independent of the initial conditions. However, for $U \geq 12$–14 m/s, multiple LCOs may occur and the initial conditions determine which LCO actually occurs.

Because of the low-level flow turbulence in the wind tunnel, the exact experimental initial conditions are continually changing and are therefore not known precisely. Also, as shown in Figs. 13 and 14 for different free-play gaps, the nondimensionalized response amplitude has a detectable difference for the experimental data, but has essentially the same value for the theory.

D. Results for the Gust Response

To obtain a more meaningful correlation between theory and experiment, the gust field is measured and quantitatively calibrated before the aeroelastic airfoil model test. For details of the gust field measurement, see [16]. Figure 15a shows the measured gust angle of attack α_g vs gust excitation frequency (in hertz) for the flow velocities of $U = 10$, 18.5, and 28 m/s which are considered in the theoretical and experimental analysis. In this figure, an open circle indicates the measured first and second harmonic components for the flow velocity $U = 10$ m/s, and the filled circle and open triangle indicate the measured values for $U = 18.5$ and 28 m/s, respectively. The solid lines are least-square curve fittings of the experimental data. A formula based upon the measured experimental gust angle of attack is constructed as

$$\alpha_g(t) = \alpha_{g1} \sin \omega_g t + \alpha_{g2} \sin(2\omega_g t + \Delta\phi) \tag{17}$$

Equation (17) is used as a gust excitation to calculate the gust response for comparison with the experimental results where α_{g1} and α_{g2} are the first and second harmonic gust amplitudes of the gust excitation. A phase difference between the first and second gust frequencies is $\Delta\phi$. It is difficult to measure this phase angle for the present RSC gust generator. Here, we assume $\Delta\phi = 0$ as an approximation.

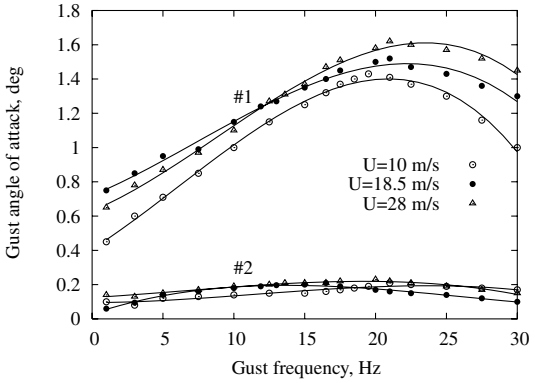

a) Gust angle vs. frequency

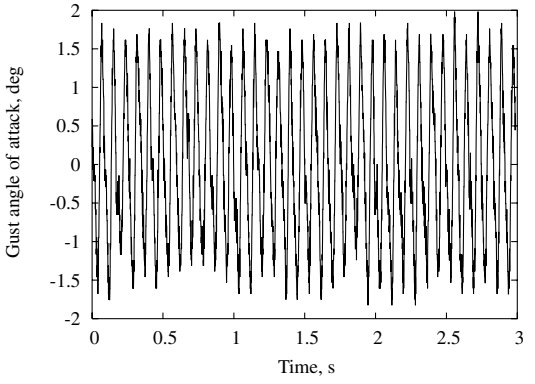

b) Time history ω_g=11.9 Hz

Fig. 15 Gust angle: a) angle of attack vs gust frequency, and b) time history for $U = 18.5$ m/s.

A typical gust time history for the flow velocity $U = 18.5$ m/s and gust frequency $\omega_g = 11.9$ Hz is shown in Fig. 15b. For the theoretical gust load analysis, a frozen gust assumption is used. For the frozen gust x, t are coordinates fixed with respect to airfoil and x', t' are coordinates fixed with respect to the atmosphere or fluid. The gust field is given by

$$w_g(x') = w_g(x - Ut)$$

Because x and t only appear in the preceding combination, we may consider the alternative functional form

$$w_g = w_g\left(t - \frac{x}{U}\right)$$

We assume that, at $t = t_0$, the leading edge of the airfoil has a gust velocity

$$w_{gl} = w_g\left(t_0 + \frac{b}{U}\right) \qquad (x = -b)$$

and at the trailing edge of the airfoil, the gust velocity is

$$w_{gt} = w_g\left(t_0 - \frac{b}{U}\right) \qquad (x = b)$$

If the gust is known as a discrete time series with a constant sampling time step length Δt, the gust at any chordwise position of the airfoil x_j is

$$w_{gc}(t_0) = w_g\left(t_0 + \frac{x_j}{U}\right) = w_g(t_0 + j\Delta t) \tag{18}$$

where j is an integral number starting from the leading edge ($j = 1$) and ending at the trailing-edge ($j = n_s$), $n_s = 2b/U\Delta t$.

At $t = t_0$, the w_{gn} coefficients of Eq. (13) can be determined by

$$w_{g0}(t_0) = \frac{1}{\pi}\int_o^\pi w_{gc}(t_0, x)\, \mathrm{d}\phi = \frac{1}{b\pi}\sum_{j=1}^{n_s} \frac{w_{gc}(t_0, x_j)\Delta x}{\sin(\cos^{-1}\phi_j)} \tag{19}$$

where $\cos\phi = x/b$, $\Delta x = U\Delta t$, $x_j = j\Delta x$, and $\phi_j = (x_j - b)/b$,

$$\begin{aligned} w_{gn}(t_0) &= \frac{2}{\pi}\int_o^\pi w_{gc}(t_0, x)\cos n\phi\, \mathrm{d}\phi \\ &= \frac{2}{b\pi}\sum_{j=1}^{n_s} \frac{w_{gc}(t_0, x_j)\cos(n\cos^{-1}\phi_j)\Delta x}{\sin(\cos^{-1}\phi_j)} \end{aligned} \tag{20}$$

Thus, $w_{g0}(t_0)$ and $w_{gn}(t_0)$ can be determined using a standard numerical integration code. When we use a time integral method to solve the nonlinear equations, those coefficients need to be evaluated at each time step.

In the present theoretical and experimental correlation study, the flow velocity is set to be $U = 18.5$ m/s. The initial pitch angle α_0 is set to 0, 2, and 4 deg. The free-play gap angle is set to $\delta = 1.06$ deg. The gust frequency varies from 2.8 to 25.2 Hz. This is achieved by controlling the cylinder speed of the RSC gust generator.

Figures 16a–16c, respectively, show the plunge, pitch, and flap frequency response for a flow velocity $U = 18.5$ m/s and the free-play gap is zero ($\delta = 0$). The gust loads used in the theoretical analysis are given by the gust angle of attack frequency response for $U = 18.5$ m/s as shown in Fig. 15. The experimental results are shown by an open circle for initial pitch angle $\alpha_0 = 0$, an open triangle for $\alpha_0 = 2$ deg, and an x for $\alpha_0 = 4$ deg. The theoretical results are shown by a solid line. In Fig. 16a, there is a very high peak response at a certain gust frequency $\omega_g = 5$ Hz. This is near the plunge resonant frequency. The values of the peak amplitude and frequency are almost independent of the initial pitch angle. In Fig. 16b, there are two very high peaks at gust frequencies $\omega_g = 5$

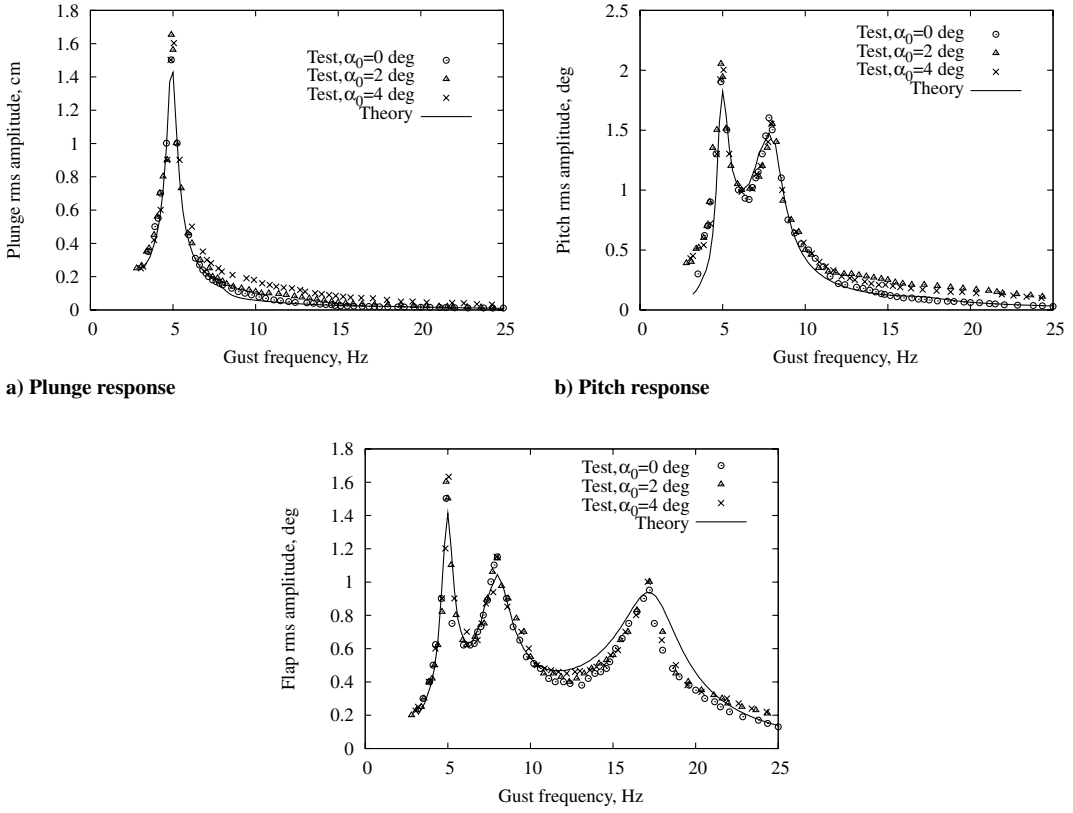

Fig. 16 Theoretical and experimental gust response for the linear airfoil model (free-play angle of $\delta = 0$ deg), initial pitch angle $\alpha_0 = 0, 2$, and 4 deg, and flow velocity $U = 18.5$ m/s.

and 7.9 Hz, respectively. These are near the plunge and pitch resonant frequencies. Also, the values of the peak amplitude and frequency are almost independent of the initial pitch angle. In Fig. 16c, there are three peaks at gust frequencies, $\omega_g = 5$, 7.9, and 17.2 Hz. They are near the plunge, pitch, and flap resonant frequencies. Again the values of the peak amplitude and frequency are almost independent of the initial pitch angle. From the linear aeroelastic theory, the theoretical results for $\alpha_0 = 0$, 2, and 4 deg are identical. These are also plotted in Fig. 16 by the solid line.

The theoretical and experimental correlations are good. There are some quantitative differences of the peak amplitude at the resonant frequencies. However, the theoretical and experimental resonant frequencies are very close.

Figures 17–19 show the rms gust response amplitudes vs the gust frequency for nonzero free play $\delta = 1.06$ deg and for several initial pitch angles $\alpha_0 = 0$, 2, and 4 deg and a flow velocity of $U=$ 18.5 m/s. Figures 17a, 18a, and 19a show the plunge response. Figures 17b, 18b, and 19b are for the pitch response. Figures 17c, 18c, and 19c show the flap response. The theoretical and experimental results are shown by an open circle and a filled circle, respectively.

Comparing the plunge response for different initial pitch angles, as shown in Figs. 17a, 18a, and 19a, it is found that there is a very high peak response at a certain gust frequency $\omega_g = 5.1$ Hz. This is near the plunge resonant frequency. The values of the peak frequency are almost independent of the initial pitch angle, but the peak amplitude has a small difference. The peak amplitude increases as the initial pitch angle increases. Also, there is a smaller peak near $\omega_g = 14$ Hz for $\alpha_0 = 0, 2$ deg and near $\omega_g = 7$ Hz for $\alpha_0 = 4$ deg. There is a very good correlation between theory and experiment in the plunge response.

Comparing the pitch response for different initial pitch angles, as shown in Figs. 17b, 18b, and 19b, it is found that there are two peak responses at gust frequency $\omega_g = 5.1$ and 8.0 Hz, respectively. They are near the plunge and pitch resonant frequencies. Also, the values of the peak frequencies are independent of the initial pitch angle. Both the plunge and pitch peak amplitudes increase as the initial pitch angle increases. In the higher gust frequency range, the rms amplitude for $\alpha_0 = 4$ deg is smaller than those for $\alpha_0 = 0$, 2 deg. Also, there is a smaller peak near $\omega_g = 14$ Hz for $\alpha_0 = 0, 2$ deg. The two theoretical peak frequencies and amplitudes are independent of the initial pitch angle. There is a reasonably good correlation between theory and experiment in the pitch response.

Comparing the flap response for different initial pitch angles, as shown Figs. 17c, 18c, and 19c, it is found that there are two obvious peak responses at gust frequencies $\omega_g = 5.1$ and 7.9 Hz which correspond to the plunge and pitch resonant responses. The peak frequencies are independent of the initial pitch angle and both the plunge and pitch peak amplitudes increase as the initial pitch angle increases. The other less obvious peak is located at frequency $\omega_g =$ 14.5 Hz for $\alpha_0 = 0$, 2 deg, and a jump in response occurs at this frequency. Above this frequency, the flap response amplitude has a small response at a near constant value, 1.25 deg. For $\alpha_0 = 4$ deg, the less obvious peak is located at frequency $\omega_g = 13.5$ Hz, and a jump in response occurs at this frequency. The flap response decreases as the gust frequency increases. The two obvious peak responses at gust frequencies $\omega_g = 5.1$ and 7.9 Hz are also found in the theoretical prediction. The other less obvious peak is located at about frequency $\omega_g = 12$ Hz for $\alpha_0 = 0$, 2, and 4 deg, and a jump in response occurs at this frequency. Above this frequency, the flap has a small response. For $\alpha_0 = 2$ deg, there is an another jump in response at a frequency of 15.5 Hz for the theoretical prediction. Above this frequency, the flap response amplitude is smaller than the free-play gap angle.

For additional details of the gust response behavior with an initial pitch angle $\alpha_0 = 2$ deg, we present typical time histories and FFT analysis of the flap motion for a flow velocity of $U = 18.5$ m/s and the frequencies $\omega_g = 4.75$, 7.7, and 17.25 Hz. These theoretical and experimental results are shown in Figs. 20–22. As shown in the flap gust response of Figs. 20 and 21, in addition to the dominant gust amplitudes at gust frequencies of 4.75 and 7.7 Hz, the second

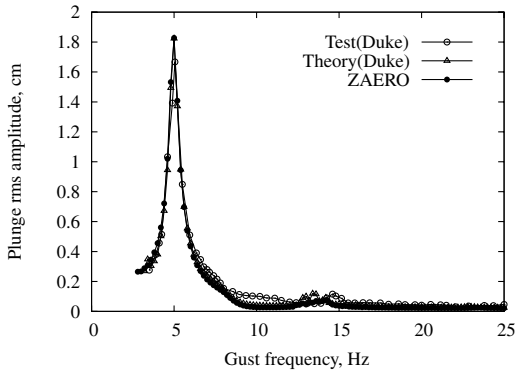

a) Plunge response

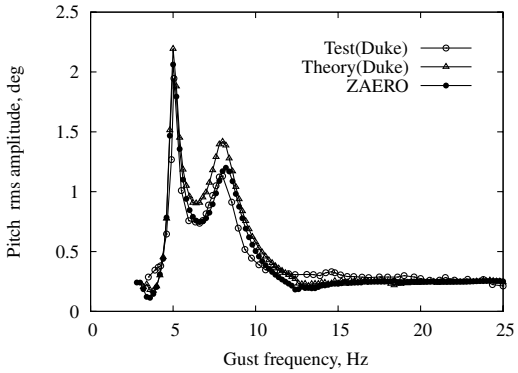

b) Pitch response

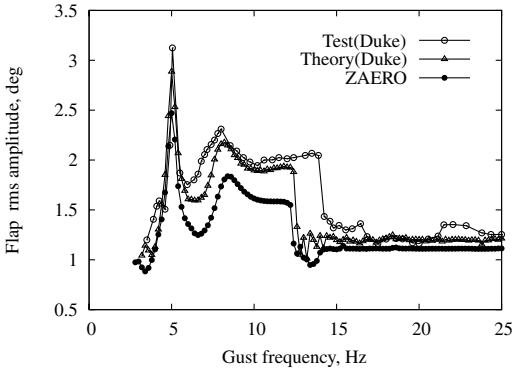

c) Flap response

Fig. 17 Theoretical and experimental gust response for free-play angle of $\delta = 1.06\,\mathrm{deg}$, initial pitch angle $\alpha_0 = 0\,\mathrm{deg}$, and flow velocity $U = 18.5\ \mathrm{m/s}$.

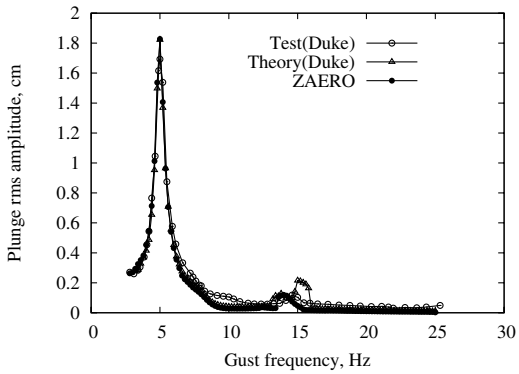

a) Plunge response

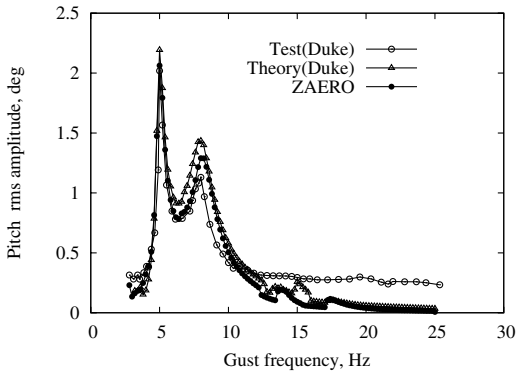

b) Pitch response

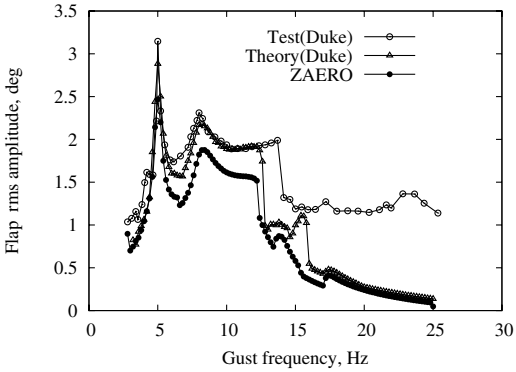

c) Flap response

Fig. 18 Theoretical and experimental gust response for free-play angle of $\delta = 1.06\,\mathrm{deg}$, initial pitch angle $\alpha_0 = 2\,\mathrm{deg}$, and flow velocity $U = 18.5\ \mathrm{m/s}$.

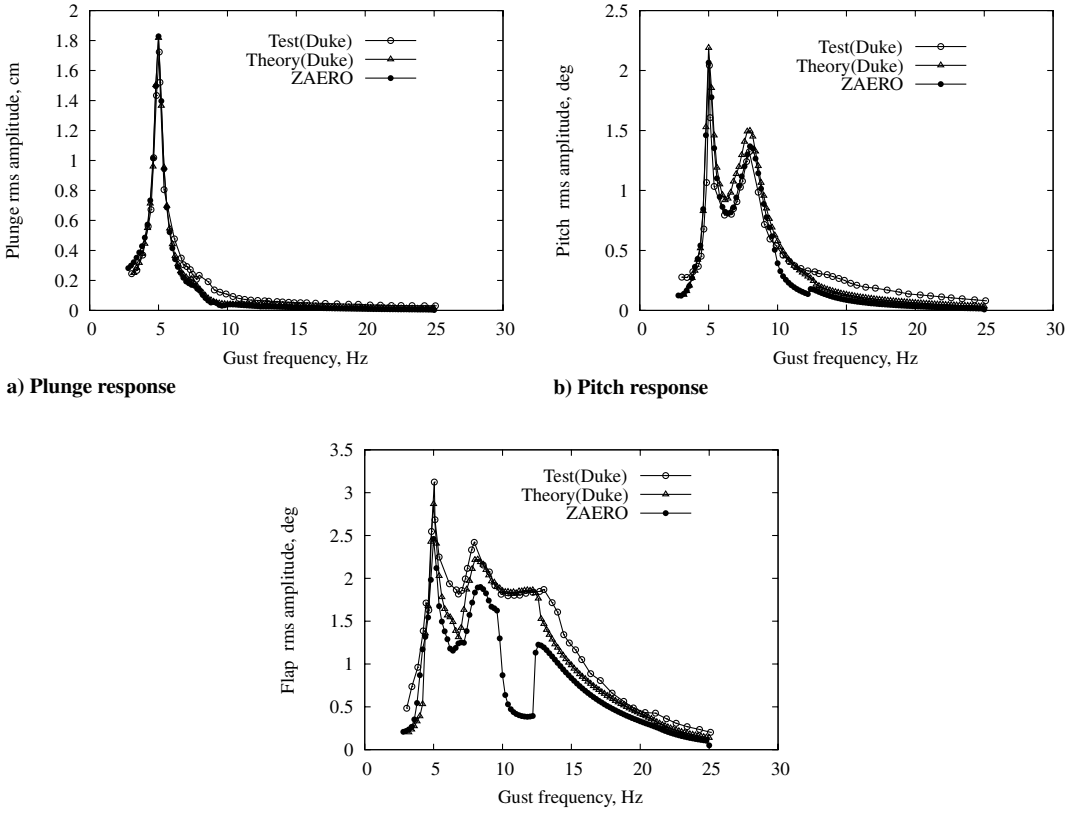

a) Plunge response

b) Pitch response

c) Flap response

Fig. 19 Theoretical and experimental gust response for free-play angle of $\delta = 1.06\,\mathrm{deg}$, initial pitch angle $\alpha_0 = 4\,\mathrm{deg}$, and flow velocity $U = 18.5\ \mathrm{m/s}$.

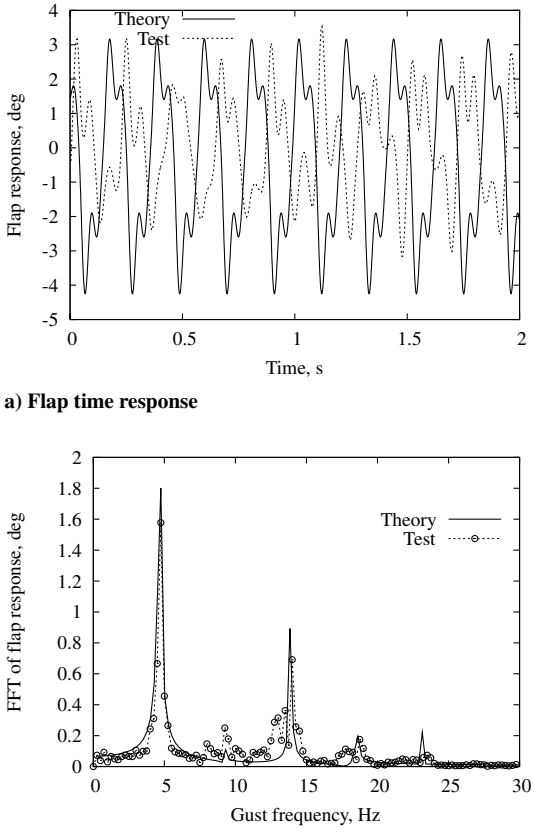

a) Flap time response

b) FFT of flap time response

Fig. 20 Theoretical and experimental time history and FFT analysis for a free-play angle of $\delta = 1.06\,\mathrm{deg}$ and initial pitch angle $\alpha_0 = 2\,\mathrm{deg}$, gust frequency $\omega_g = 4.75$ Hz, and flow velocity $U = 18.5\ \mathrm{m/s}$.

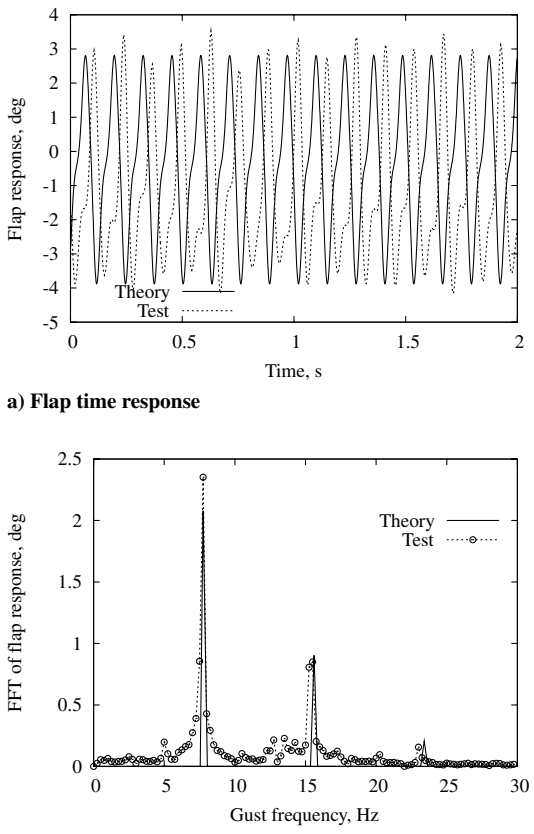

a) Flap time response

b) FFT of flap time response

Fig. 21 Theoretical and experimental time history and FFT analysis for a free-play angle of $\delta = 1.06\,\mathrm{deg}$ and initial pitch angle $\alpha_0 = 2\,\mathrm{deg}$, gust frequency $\omega_g = 7.75$ Hz, and flow velocity $U = 18.5\ \mathrm{m/s}$.

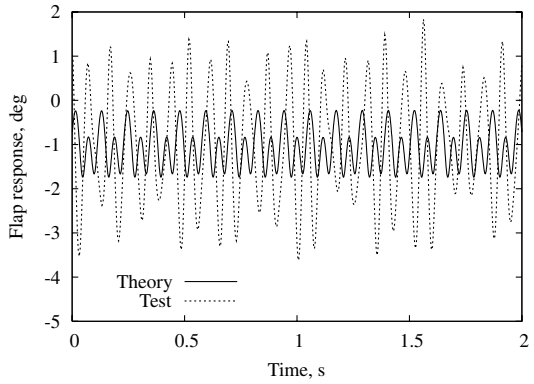

a) Flap time response

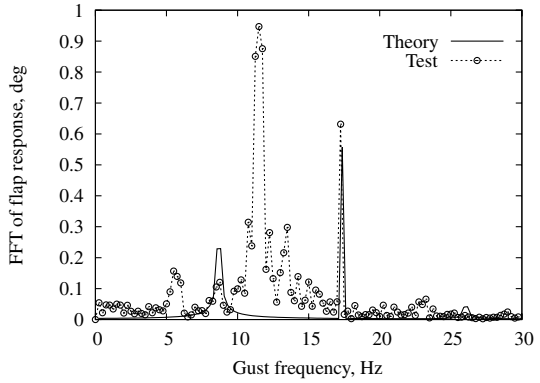

b) FFT of flap time response

Fig. 22 Theoretical and experimental time history and FFT analysis for a free-play angle of $\delta = 1.06$ deg and initial pitch angle $\alpha_0 = 2$ deg, gust frequency $\omega_g = 17.25$ Hz, and flow velocity $U = 18.5$ m/s.

harmonic gust responses at $\omega_g = 2 \times 4.75$ and $\omega_g = 2 \times 7.7$ Hz are present in both the theory and experiment. This is because there is a second harmonic gust frequency in the total input gust loads, as shown in Fig. 15a.

As shown in the flap gust response of Fig. 20 for $\omega_g = 17.25$ Hz, the theoretical flap rotation angle motion is less than $\pm\delta$ and the equilibrium position of the flap vibration is near -1.06 deg. This means the flap motion is in a "oneside-flap stiffness" state. Comparing FFT analysis of the theoretical and experimental time histories, the theoretical dominant response peak is at the gust frequency $\omega_g = 17.25$ Hz, but the experimental dominant response peak is at the frequency of 11.5 Hz, not at the gust frequency $\omega_g = 17.25$ Hz. The peak frequency of 11.5 Hz is the LCO frequency, as shown in Figs. 7c and 7d. This suggests that, when the gust excitation is at higher gust frequency, the system response may display a predominantly LCO behavior. It is possible that the response in this range is dependent on initial conditions, but this has yet to be studied systematically.

IV. Conclusions

A theoretical and experimental aeroelastic study of a typical airfoil section with control surface free play for nonzero angle of attack in low subsonic flow has been presented in this paper. The study includes the flutter and limit cycle oscillation behavior and the nonlinear response excited by periodic gust loads.

Comparing the results for the two different free-play gaps but the identical ratio of the initial pitch angle to the half free-play gap and two different initial conditions, it is found that the following conclusions may be drawn.

1) The responses for the two free-play angles have similar LCO amplitudes when they are normalized by the free-play angle.

2) The flow velocity corresponding to a jump in the LCO response from a lower frequency oscillation to a higher frequency oscillation is modestly higher for a free-play gap of 2×1.06 compared to that for 2×2.12. However, this flow velocity is significantly dependent on the prescribed initial pitch angle α_0.

3) The effect of the initial pitch angle on the LCO amplitude is significant. When the ratio of the initial pitch angle to the half free-play gap is larger than 3×0.943 for both $\delta = 1.06$ and $\delta = 2.12$, the flow velocity range for the LCO becomes much smaller, and the LCO disappears entirely for a ratio of greater than 4×0.943.

4) The effect of the initial conditions on the LCO amplitude is quite significant for sufficiently high flow velocities beyond the lower flow velocity at which LCO begins. Not surprisingly, correlations of computations and experiments are more difficult in this higher flow velocity range.

5) If the only nonlinearity in the model were that due to structural free play, then the scaled (by free-play angle) nondimensional response for both free-play angles would be the same. The differences that do exist and the differences between the test data and theoretical computations may be due to aerodynamic nonlinearities at the higher angles of attack and free play.

The following conclusions may be drawn for the gust response.

1) For the linear structural model (free-play gap is zero, $\delta = 0$), the gust response is essentially independent of the initial pitch angle for the present case of an initial angle of attack $\alpha_0 \leq 4$ deg.

2) For a free-play gap $\delta = 1.06$ deg, the resonant frequency of plunge response and resonant frequency of the pitch response are essentially independent of the initial pitch angle for $\alpha_0 \leq 4$ deg, and the peak amplitudes corresponding to these resonant frequencies change modestly for flow velocities well below the linear (no free play) flutter velocity. This is true for both the experiment and the computations.

3) The larger effect of the initial pitch angle occurs in the flap response. A jump in flap response from a higher amplitude to a lower amplitude may occur and a larger initial pitch angle can lead to a very small amplitude response in the higher frequency range.

The fair to good quantitative agreement between theory and experiment verifies that the present method has reasonable accuracy and good computational efficiency for both the flutter/LCO and nonlinear gust response analysis.

References

[1] Conner, M. D., Tang, D. M., Dowell, E. H., and Virgin, L. N., "Nonlinear Behavior of a Typical Airfoil Section with Control Surface Freeplay: A Numerical and Experimental Study," *Journal of Fluids and Structures*, Vol. 11, No. 1, 1997, p. 89. doi:10.1006/jfls.1996.0068

[2] Tang, D. M., Conner, M. D., and Dowell, E. H., "A Reduced Order Aerodynamic Model and its Applications to a Nonlinear Aeroelastic System," *Journal of Aircraft*, Vol. 35, No. 2, 1998, pp. 332–338. doi:10.2514/2.2304

[3] Tang, D. M., Dowell, E. H., and Virgin, L. N., "Limit Cycle Behavior of an Airfoil with a Control Surface," *Journal of Fluids and Structures*, Vol. 12, No. 7, 1998, pp. 839–858. doi:10.1006/jfls.1998.0174

[4] Trickey, S. T., Virgin, L. N., and Dowell, E. H., "The Stability of Limit Cycle Oscillations in a Nonlinear Aeroelastic System," *Proceedings of the Royal Society of London, Series A: Mathematical, Physical, and Engineering Sciences*, Vol. 458, No. 2025, 2002, pp. 2203–2226. doi:10.1098/rspa.2002.0965

[5] Liu, L., and Dowell, E. H., "Harmonic Balance Approach for an Airfoil with a Freeplay Control Surface," *AIAA Journal*, Vol. 43, No. 4, 2005, p. 802. doi:10.2514/1.10973

[6] Tang, D. M., Kholodar, D., and Dowell, E. H., "Nonlinear Aeroelastic Response of an Airfoil Section with Control Surface Freeplay to Gust Loads," *AIAA Journal*, Vol. 38, No. 9, 2000, pp. 1543–1557. doi:10.2514/2.1176

[7] Tang, D. M., Henri, P. G., and Dowell, E. H., "Study of Airfoil Gust Response Alleviation Using an Electro-Magnetic Dry Friction Damper, Part 1: Theory," *Journal of Sound and Vibration*, Vol. 269, Nos. 3–5, 2004, pp. 853–874. doi:10.1016/S0022-460X(03)00180-9

[8] Tang, D. M., Henri, P. G., and Dowell, E. H., "Study of Airfoil Gust Response Alleviation Using an Electro-Magnetic Dry Friction Damper,

Part 2: Experiment," *Journal of Sound and Vibration*, Vol. 269, Nos. 3–5, 2004, pp. 875–897.
doi:10.1016/S0022-460X(03)00181-0

[9] Cox, D. E., "Control Design for Parameter Dependent Aeroelastic System," Ph.D. Thesis, Duke Univ., Durham, NC, 2003.

[10] Vipperman, J. S., Clark, R. L., Conner, M., and Dowell, E. H., "Experimental Active Control of a Typical Section Using a Trailing Edge Flap," *Journal of Aircraft*, Vol. 35, No. 2, 1998, pp. 224–229.
doi:10.2514/2.2312

[11] Vipperman, J. S., Clark, R. L., Conner, M., and Dowell, E. H., "Comparison of μ and H_2 Synthesized Controllers on an Experimental Typical Section," *Journal of Guidance, Control, and Dynamics*, Vol. 22, No. 2, 1999, pp. 278–285.
doi:10.2514/2.4375

[12] Frampton, K. D., and Clark, R. L., "Experimentals on Control of Limit Cycle Oscillations in Typical Section," *Journal of Guidance, Control, and Dynamics*, Vol. 23, No. 5, 2000, pp. 956–960.
doi:10.2514/2.4638

[13] Kholodar, D., and Dowell, E. H., "Behavior of Airfoil Section with Control Surface Freeplay for Nonzero Angles of Attack," *AIAA Journal*, Vol. 37, No. 5, 1999, pp. 651–653.
doi:10.2514/2.766

[14] Peters, D. A., "Finite-State Airloads for Deformable Airfoils on Fixed and Rotating Wings," *Symposium on Aeroelasticity and Fluid/Structure Interaction*, Rev. 3, American Society of Mechanical Engineers Winter Annual Mtg., AD-Vol. 44, May 1996.

[15] Peters, D. A., and Cao, W. M., "Finite State Induced Flow Models, Part I: Two-Dimensional Thin Airfoil," *Journal of Aircraft*, Vol. 32, No. 2, 1995, pp. 313–322.
doi:10.2514/3.46718

[16] Tang, D. M., Cizmas, P. G. A., and Dowell, E. H., "Experiments and Analysis for a Gust Generator in a Wind Tunnel," *Journal of Aircraft*, Vol. 33, No. 1, Jan.–Feb. 1996, pp. 139–148.
doi:10.2514/3.46914

E. Livne
Associate Editor